

Grommet: an N -body code for high-resolution simulations of individual galaxies

John Magorrian*

Rudolf Peierls Centre for Theoretical Physics, 1 Keble Road, Oxford OX1 3NP

ABSTRACT

This paper presents a fast, economical particle-multiple-mesh N -body code optimized for large- N modelling of collisionless dynamical processes, such as black-hole wandering or bar-halo interactions, occurring within isolated galaxies. The code has been specially designed to conserve linear momentum. Despite this, it also has variable softening and an efficient block-timestep scheme: the force between any pair of particles is calculated using the finest mesh that encloses them both (respecting Newton’s third law) and is updated only on the longest timestep of the two (which conserves momentum). For realistic galaxy models with $N \gtrsim 10^6$, it is faster than the fastest comparable momentum-conserving tree code by a factor ranging from ~ 2 (using single timesteps) to ~ 10 (multiple timesteps in a concentrated galaxy).

Key words:

1 INTRODUCTION

Newton’s third law is a central pillar of physics. Much of what we know about the dynamical evolution of galaxies comes from N -body simulation, but most N -body codes use approximations that break the third law. In many situations this transgression is relatively benign, but whenever one is interested in the detailed response of a galaxy to an asymmetric perturbation it is important to be able to calculate this response without breaking the third law. A well-known example of the consequences of breaking it is provided by the sinking satellite problem (Hernquist & Weinberg 1989; Weinberg 1989; Velazquez & White 1999); the dynamical friction felt by the satellite is grossly overestimated if one “pins” the centre of the host galaxy, ignoring the galaxy’s $l = 1$ dipole response. Other obvious, but as yet unsolved, examples include modelling bar-halo interactions (see McMillan & Dehnen (2005) and references therein) and the wandering of central supermassive black holes.

This paper describes the N -body code Grommet (GRavity On Multiple Meshes Economically and Transparently), which has been designed specifically to model the detailed dynamical evolution of individual galaxies without using any approximations that violate Newton’s third law. I assume that the galaxy is collisionless. It is completely described by a distribution function (DF) $f(\mathbf{x}, \mathbf{v}; t)$, which gives the (mass) density of particles in phase space, along with the potential $\Phi(\mathbf{x}; t)$ generated by this DF and any external sources. The evolution of f is governed by the col-

lisionless Boltzmann equation (CBE):

$$\frac{\partial f}{\partial t} + \mathbf{v} \cdot \nabla f + \mathbf{a} \cdot \frac{\partial f}{\partial \mathbf{v}} = 0, \quad (1)$$

where the accelerations $\mathbf{a} \equiv -\partial\Phi/\partial\mathbf{x}$. As Hernquist & Ostriker (1992) and Leeuw, Combes & Binney (1993) emphasise, in a collisionless N -body code particles are not to be thought of as representing stars or groups of stars. Instead one is using the method of characteristics to integrate (1), estimating the accelerations $\mathbf{a}(\mathbf{x})$ by Monte Carlo sampling. Of course, the shot noise in these estimates means that in practice any simulation will never be perfectly collisionless. Therefore it is important to make N as large as possible in order to minimize the effects of this noise. So, Grommet has been designed to be both fast and economical on memory.

In section 2 below I describe the multiple-mesh scheme used by Grommet to estimate accelerations. This scheme leads naturally to a momentum-conserving block-timestep integrator, as explained in section 3. I present the results of some tests in section 4 and compare Grommet’s performance against other codes*. Section 5 sums up. For completeness, I include in an Appendix an explanation of James’ (1977) method, which is used in Section 2.

2 POTENTIAL SOLVER

The task of the potential solver in a collisionless N -body code is to estimate the accelerations

$$\mathbf{a}(\mathbf{x}) = -\nabla \int \frac{G\rho(\mathbf{x}')}{|\mathbf{x} - \mathbf{x}'|} d^3x, \quad (2)$$

* E-mail: magog@thphys.ox.ac.uk

where one does not know the density distribution $\rho(\mathbf{x})$ explicitly, but instead only has a discrete sample of N particles with positions \mathbf{x}_i and masses m_i drawn from it.

2.1 Particle-mesh method

At the heart of Grommet's potential solver is the particle mesh (PM) method (Hockney & Eastwood 1988). It uses a cubical mesh, with vertices at positions \mathbf{x}_{ijk} , spaced a distance h apart. The procedure for obtaining an initial estimate of the accelerations (eq. 2) felt by each particle is as follows:

- (i) Loop over all N particles using cloud-in-cell interpolation to build up the discretized density distribution $\rho_{ijk} = \rho(\mathbf{x}_{ijk})$;
- (ii) Calculate the potential Φ_{ijk} corresponding to this ρ_{ijk} using James' (1977) method (see Appendix);
- (iii) Looping again over all N particles, use a finite-difference approximation to estimate accelerations $-\partial\Phi/\partial\mathbf{x}$ at the mesh points surrounding each particle, then interpolate the value of the acceleration at the particle's location using the same cloud-in-cell scheme employed in step (i).

Since steps (i) and (iii) use the same interpolation scheme, this procedure produces accelerations that obey Newton's third law subject to one extra condition: the finite-difference scheme in step (iii) cannot provide meaningful accelerations for particles that lie in the outermost layer of mesh cells, which means that those particles should be omitted in step (i). This seems an almost trivial point, but it is important for the refinement scheme introduced below. It turns out that for the scheme below to work properly we have to peel off the outer *two* layers of cells. I typically use meshes with 64^3 or 128^3 cells, of which then only 60^3 or 124^3 are assignable in step (i).

Apart from respecting Newton's third law, the other attractive features of the PM method are its efficiency and its linear scaling with N : the time needed to carry out step (ii) is independent of N , but for a typical mesh with 64^3 cells the overall time is dominated by the $\mathcal{O}(N)$ cost of carrying out the assignment steps (i) and (iii) once $N \gtrsim 5 \times 10^5$; similarly, the memory needed to store mesh quantities and to carry out James' method is negligible compared to that used for storing the particles' masses, positions and accelerations.

Of course, the major disadvantage of the PM method is that it does not work well for centrally concentrated mass distributions, since each particle has an effective size of order the grid spacing h .

2.2 Refinement scheme

The natural remedy of this shortcoming is to introduce finer submeshes in interesting, higher-density regions and to recalculate the accelerations for particles inside each submesh. But how best to include the effect of the parent mesh's gravity field on the accelerations calculated in each submesh and vice versa? One possibility is to solve Poisson's equation on the submesh subject to boundary conditions interpolated from the parent mesh (e.g., Anninos, Norman & Clarke 1994; Jessop, Duncan & Chau 1994). This is a key element of the widely-used family of multigrid methods (e.g., Kravtsov,

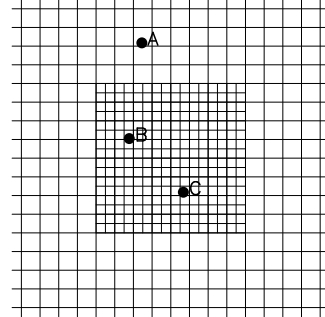


Figure 1. An example of the multiple mesh scheme used to calculate accelerations. Particles A, B and C all lie within the region covered by the outer, coarse mesh, but B and C also lie inside the fine, inner mesh. An initial estimate of the forces on all three particles comes from using the PM method on the coarse mesh. This is refined by isolating those particles within the inner mesh, recalculating their interparticle forces first using the fine mesh, then using the coarse, and adding the difference to the initial coarse-mesh estimate. Therefore, the force between A and each of B and C is obtained using the coarse mesh, but that between B and C comes from the fine mesh. In all cases Newton's third law is respected.

Klypin & Khokhlov 1997; Knebe, Green & Binney 2001), and would be straightforward to apply in Grommet using the method of equivalent charges (see Appendix). However, all of these schemes violate Newton's third law, as one can easily see by considering the force between a particle inside a submesh and another one outside.

Grommet instead uses a simplified version of the scheme proposed by Gelato, Chernoff & Wasserman (1997) (see also figure 1). The acceleration felt by each particle is calculated using a series of nested “boxes”. We start with the outermost toplevel box, which discretizes the simulation volume into, say, $n_x \times n_y \times n_z = 60^3$ assignable cells. This box, like any other box, can contain zero, one or more subboxes. Each subbox contains two meshes: a coarse one composed of an $(n_x/2) \times (n_y/2) \times (n_z/2)$ subblock of the parent's cells, and a fine one that covers the same subblock twice as finely in each direction, with $n_x \times n_y \times n_z$ cells.

For the most common situation in which each box contains no more than one subbox, the acceleration at any position \mathbf{x} is given by the sum over all boxes,

$$\mathbf{a}(\mathbf{x}) = \sum_j \mathbf{a}_j(\mathbf{x}), \quad (3)$$

where the contribution from the j^{th} box,

$$\mathbf{a}_j(\mathbf{x}) = \mathbf{a}_j^+(\mathbf{x}) - \mathbf{a}_j^-(\mathbf{x}), \quad (4)$$

is the difference between accelerations calculated using the PM method on the box's fine (+) and coarse (-) meshes, simply ignoring any particles that lie outside. Of course, the outermost toplevel box ($j = 0$) has no coarse mesh, so $\mathbf{a}_0^- = 0$. In this scheme the acceleration between any two particles is calculated using the box with the finest mesh spacing that encloses them both and Newton's third law is obeyed to machine precision. This last feature comes at a cost though: the acceleration (3) is discontinuous at box boundaries, a point to which I return in section 4 below.

Sometimes one might want to refine a region that can-

not be enclosed within a single subbox. If one simply tiles the region using, say, two abutting subboxes, the force between particles located at either side of the boundary between them will be calculated using the coarse parent mesh, which is usually not desirable. The solution is to let the subboxes overlap by a few mesh cells and then correct eq. (3) for the double counting of particles in the overlap region by introducing a third subbox whose boundaries are given by the intersection of the two overlapping subboxes and subtracting the accelerations (4) obtained in this new subbox. In contrast, Gelato, Chernoff & Wasserman (1997) introduce a buffer zone around each box and treat particles in the buffer zone differently from the rest. Their scheme violates Newton's third law.

I have deliberately omitted any automated scheme for deciding where and when to introduce subboxes; these schemes inevitably break time-reversibility, and, for the type of problem the code was designed for, I expect that the user will already have a much better idea of how best to place boxes.

3 MOVING PARTICLES

The characteristic equation of the CBE is

$$\frac{dt}{1} = \frac{dx}{v} = \frac{dv}{a}, \quad (5)$$

where the accelerations $a(\mathbf{x}, t)$ depend on the DF f through equ. (2). The most straightforward and widely used way of following the characteristics is by using a leapfrog integrator. The (fixed-timestep) leapfrog produces an approximate solution to (5) that respects many of its important symmetries; it is symplectic, reversible in time and conserves linear momentum, provided the accelerations are obtained using a potential solver that respects Newton's third law.

An unattractive feature of the leapfrog is that it uses the same fixed timestep for all particles. Consider a deeply plunging radial orbit in a model galaxy with a central density cusp or black hole. Integrating this orbit accurately near pericentre requires a very small timestep, which, in the standard leapfrog scheme, means that all other particles have to be integrated using the same small timestep, even those on loosely bound circular orbits. This can be prohibitively expensive, since it involves calculating the full set of accelerations $a(\mathbf{x}, t)$ for all particles at every timestep.

Grommet uses a block-timestep scheme to improve efficiency. Each of the boxes of section 2 above has an associated timestep, which can be chosen to be either equal to that of its parent box or a factor of two shorter. Broadly speaking, a particle's position and velocity are updated using the shortest timestep of any of the boxes enclosing it, but the force between any pair of particles is updated only on the timestep of the longest particle, thus conserving linear momentum. The rest of this section makes this somewhat vague description more precise.

3.1 A block-timestep leapfrog integrator

Recall that a leapfrog integrator with a single, fixed timestep τ corresponds to motion in a time-dependent Hamiltonian

(e.g., Wisdom & Holman 1991)

$$H = T + \sum_{k=-\infty}^{\infty} \delta_{\epsilon} \left(k - \frac{t}{\tau} \right) V(\mathbf{x}_1, \dots, \mathbf{x}_N), \quad (6)$$

where $T \equiv \frac{1}{2} \sum_i m_i v_i^2$ is the kinetic energy of all the particles and $\delta_{\epsilon}(x) \equiv \frac{1}{2}(\delta(x - \epsilon) + \delta(x + \epsilon))$ with $0 < \epsilon \ll 1$. The periodic comb of delta functions turns on the potential energy $V(\mathbf{x}_1, \dots, \mathbf{x}_N)$ only at times $t = (k \pm \epsilon)\tau$ for integer k . Integrating the resulting equations of motion from time $t = k\tau$ to $t = (k+1)\tau$ yields

$$\mathbf{v}_i(k + \frac{1}{2}) = \mathbf{v}_i(k) + \frac{1}{2}\tau \mathbf{a}_i(k) \quad (7)$$

$$\mathbf{x}_i(k + 1) = \mathbf{x}_i(k) + \tau \mathbf{v}_i(k + \frac{1}{2}) \quad (8)$$

$$\mathbf{v}_i(k + 1) = \mathbf{v}_i(k + \frac{1}{2}) + \frac{1}{2}\tau \mathbf{a}_i(k + 1) \quad (9)$$

where the accelerations $\mathbf{a}_i(k) \equiv -\partial V/m_i \partial \mathbf{x}_i$ evaluated at time $t = k\tau$. This is just the sequence of steps for the kick-drift-kick form of the leapfrog: the potential is turned on briefly just after $t = k\tau$ resulting in a "kick" (denoted K) to the particles' velocities; the particles then "drift" (D) along at their new velocities until the potential turns on again just before $t = (k+1)\tau$, at which point they receive another kick. The drift-kick-drift form of the leapfrog can be obtained by adding $\frac{1}{2}$ to the argument of the delta functions or, alternatively, by integrating the equations of motion from $(k - \frac{1}{2})\tau$ to $(k + \frac{1}{2})\tau$ instead.

Another way of looking at each of these versions of the leapfrog is to consider them as compositions of the two time-asymmetric first-order symplectic integrators (each applied left to right), $K(\tau/2)D(\tau/2)$ and $D(\tau/2)K(\tau/2)$, whose first-order error terms cancel (e.g., Saha & Tremaine 1992). In the following I write the leapfrogs as the sequence of operations $KDDK$ and $DKKD$, dropping the $(\tau/2)$ arguments.

Returning to the Hamiltonian (6), the potential energy $V(\mathbf{x}_1, \dots, \mathbf{x}_N)$ is a sum of pairwise interactions V_{ij} ,

$$V = \sum_i \sum_{j < i} V_{ij}(\mathbf{x}_i, \mathbf{x}_j), \quad (10)$$

the derivatives of V_{ij} being given by the multiple-mesh scheme of section 2. Instead of turning on every V_{ij} at every timestep, let us consider the alternative Hamiltonian

$$H = T + \sum_{l=0}^{l_{\max}} \sum_{k=-\infty}^{\infty} \delta_{\epsilon} \left(k - \frac{t}{2^{-l}\tau_0} \right) V_l(\mathbf{x}_1, \dots, \mathbf{x}_N), \quad (11)$$

where l_{\max} is the maximum timestep refinement level and the potential is split into a sum of terms

$$V_l = \sum_i \sum_{j < i} c_l(l_i, l_j) V_{ij}(\mathbf{x}_i, \mathbf{x}_j), \quad (12)$$

each of which is turned on only at times $t = 2^{-l}k\tau_0$. Here l_i is the timestep level of the i^{th} particle and the function

$$c_l(l_1, l_2) \equiv \begin{cases} 1, & \text{if } \min(l_1, l_2) = l, \\ 0, & \text{otherwise,} \end{cases} \quad (13)$$

ensures that each pairwise interaction appears in $V \equiv \sum_l V_l$ only once, for l given by the longest timestep of the pair.

Integrating the equations of motion for this new Hamiltonian (11) results in a nested sequence of $KDDK$ leapfrog steps, as shown in figure 2. It is obvious that this conserves



Figure 2. The sequence of steps for motion in the Hamiltonian (11) with two levels of timestep refinement. For any given timestep level l , the K operation “kicks” particles on levels l and higher, applying to each an impulse $\frac{1}{2}\tau_l \cdot (-\partial V_l / \partial \mathbf{x})$, where $\tau_l = 2^{-l}\tau_0$ is the timestep of particles on level l and V_l is given by equation (12). These impulses change the particles’ velocities, but not their positions. They do not change the particles’ total linear momentum. The D operation “drifts” particles on level l forward for a time $\frac{1}{2}\tau_l$, changing their positions but not their velocities.

linear momentum. It is not reversible in time though: particles entering or leaving a box can change timestep levels, but this level depends only on the particle’s position at the start of the step. This change in timestep also breaks symplecticity. Therefore, one should regard the Hamiltonian (11) merely as a convenient source of a set of rules for moving particles in a momentum-conserving fashion.

3.2 When should particles change timestep?

Of course, the pseudo-Hamiltonian formulation above has nothing to say about exactly when a particle should change timestep. Each particle undergoes a sequence of $KDDK$ leapfrog steps, but during the course of any one of these steps a particle can cross a box boundary, possibly changing its timestep level. I impose the natural restriction that the D and K operations in each individual $KDDK$ step are all carried out using same timestep. In this subsection I address the question of how to choose between the two possible timesteps used to follow a particle across a box boundary.

As illustration, take a test particle moving in the potential of a singular isothermal sphere. The particle is on an almost radial orbit with (in dimensionless units) pericentre radius 0.1, apocentre radius 2.67 and period $P = 5.67$. The results of integrating its orbit using each of the $DKKD$ and $KDDK$ leapfrogs with fixed timestep $\tau_{\text{leap}} = P/250$ are plotted on the left panel of figure 3. These are both reversible, so the particle’s energy shows no long-term drift in time.

Now consider the block-timestep scheme defined by the following sequence of nested boxes. When the particle is in the innermost box, $|\mathbf{x}| < 0.25$, it moves with timestep τ_{leap} . Outside this box but inside $|\mathbf{x}| < 0.5$, it moves with timestep $2\tau_{\text{leap}}$. For $0.5 < |\mathbf{x}| < 1$ the timestep is $4\tau_{\text{leap}}$, while for $|\mathbf{x}| > 1$ the timestep is $8\tau_{\text{leap}}$. Simply choosing the particle’s timestep based on its position at the start of each $KDDK$ step is clearly not reversible, and the middle panel of figure 3 shows that this naive scheme has poor long-term behaviour.

An obvious idea is then to choose the timestep based on the particle’s position at the “middle” of each $KDDK$ step. Of course, the particle’s position at the middle of a step itself depends on the trial timestep chosen, so this scheme does not, in general, yield a unique answer and will therefore result in an integrator that is not perfectly reversible. Nevertheless, let us follow Quinn et al. (1997) and introduce a “Select” operator $S(\tau)$ which tests whether a proposed timestep τ is acceptable for the particle’s position. Then a sequence such as $DDSKK$ is to be understood as returning $DDKK$ if $S(\tau)$ is true after the two drifts have been applied; otherwise it returns the empty identity sequence, with the

particle’s position and velocity restored to their original pre- DD values.¹ The naive integrator of the last paragraph can clearly be obtained by repeated application of the sequence $SKDDK$ working downwards from the longest timestep until one is accepted.

Based on the $DKKD$ leapfrog, Quinn et al. (1997) propose an integrator built around the “palindromic” sequence $DKSKD$. Since S depends only on the particle’s position which is unchanged by K , this is equivalent to the cheaper-to-test sequence $DSKKD$. The obvious analogue for a $KDDK$ integrator is $KDSDK$. Both can be written $\langle \text{Move1} \rangle S \langle \text{Move2} \rangle$, where $\langle \text{Move1} \rangle$ and $\langle \text{Move2} \rangle$ are each composed of some combinations of kicks and drifts. Then taking suitably loose definition of the select operator S , a straightforward recursive algorithm for advancing a particle using either of these schemes is as follows:

```

Step( $l$ ,  $l_P$ ,  $\tau$ ):
  if  $l > l_{\text{max}}$ : return
  if  $l_P$  is unassigned:
    Move1( $\tau$ )
    set  $b = \text{BestLevel}(P)$ 
    if  $b \leq l$ : set  $l_P = l$ 
    Undo Move1( $\tau$ )
    Move1( $\tau$ ) if  $l_P = l$ 
    Step( $l + 1, l_P, \tau/2$ )
    Move2( $\tau$ ) if  $l_P = l$ 
    Step( $l + 1, l_P, \tau/2$ )
    if  $l_P = l$ : unassign  $l_P$ 

```

The timestep level l of the outermost box is zero and increases by one for each halving of the timestep, up to a maximum value l_{max} . The particle itself is advanced at timestep level l_P , this level being chosen by repeated trial applications of the $\langle \text{Move1} \rangle$ operation; the call to $\text{BestLevel}(P)$ returns the maximum timestep level of the set of boxes enclosing the particle. Once l_P has been assigned the particle completes a full $\langle \text{Move1} \rangle \langle \text{Move2} \rangle$ step, after which l_P is unassigned, leaving the particle free to be given a different timestep.

The results of applying this algorithm to the $KDSDK$ and $DKSKD$ sequences are plotted in the middle panel of Figure 3, showing that it introduces no significant long-term drift in the particle’s energy. It is obvious that the algorithm should work similarly well for for any pair of operations for which $\langle \text{Move2} \rangle(-\tau)$ undoes the effects of $\langle \text{Move1} \rangle(\tau)$.

The attraction of the $KDSDK$ integrator is diluted by the requirement to perform an expensive kick operation before testing whether a given timestep is acceptable. So, for

¹ Notice that I follow Quinn et al. (1997) and write the elements of each sequence from left to right in the order in which they are applied.

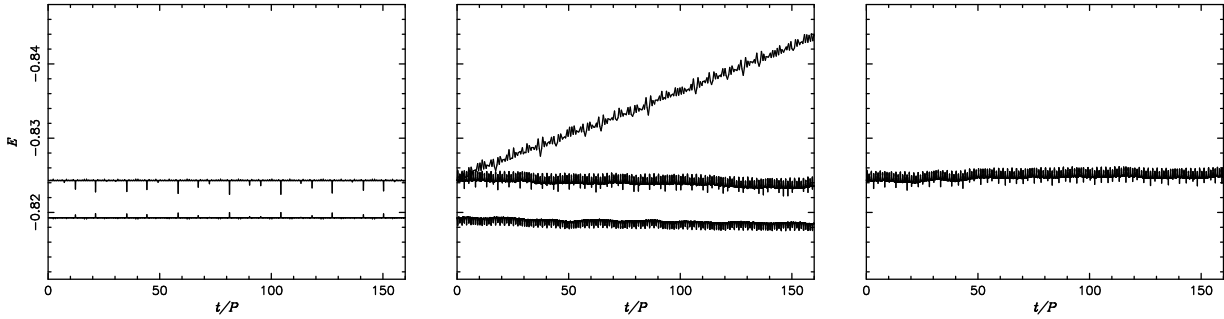


Figure 3. Variation in energy with time for a test particle moving on an almost radial orbit in the potential of a singular isothermal sphere obtained using different integration schemes. The left panel shows results for the standard fixed-timestep *DKKD* (top) and *KDDK* (bottom) leapfrogs, the latter being offset vertically for clarity. The middle shows results for the corresponding palindromic block-timestep *DSKKD* (Quinn et al. 1997) and *KDSKD* integrators (upper and lower broadly horizontal curves), along with the naive *SKDDK* integrator (diagonal curve). The right panel shows the *DSD⁻¹KDDK* alternative to the *KDSKD* integrator used by Grommet.

Grommet I use a more economical alternative which simply omits the initial kick, giving *DSD⁻¹KDDK* where $D^{-1} \equiv D(-\tau/2)$ (i.e., $\langle \text{Move1} \rangle = D$, $\langle \text{Move2} \rangle = D^{-1} \text{KDDK}$). The results, plotted on the right panel of Figure 3, are not identical to those obtained using the full sequence, but they show similarly good long-term behaviour.

3.3 A momentum-conserving, almost-reversible block-timestep algorithm

Putting this timestep-selection scheme together with the pseudo-Hamiltonian equations of motion derived from equation (11) results in the following algorithm for integrating N bodies:

```

NBodyStep( $l, \tau, \{s_i\}$ ):
  set  $s_{l+1} = \text{Shuffle}(l, s_l, \tau)$ 
  Kick( $\tau/2$ ) [ $s_l \dots N$ ]
  if  $l < l_{\max}$ :
    Kick( $-\tau/2$ ) [ $s_{l+1} \dots N$ ]
    NBodyStep( $l+1, \tau/2, \{s_i\}$ )
    CompleteSteps( $l+1, \tau/2, \{s_i\}$ )
  Drift( $\tau$ ) [ $s_l \dots s_{l+1}$ ]
  if  $l < l_{\max}$ :
    NBodyStep( $l+1, \tau/2, \{s_i\}$ )
  if  $l = 0$ :
    CompleteSteps( $l, \tau, \{s_i\}$ )

```

This progressively rearranges the list of particles, with those having the longest timesteps (level $l = 0$) being placed at the head of the list and, eventually, the level- l_{\max} particles migrating to the end. At each invocation particles at positions 0 to $s_l - 1$ have already been assigned to lower (longer) timestep levels. The call to `Shuffle` works through the unsorted particles $s_l \dots N$ and rearranges them such that particles $s_l \dots s_{l+1}$ are best moved on timestep l or lower. Once a particle has been assigned a timestep in this way, it will always complete a full *KDDK* step. On completion, it becomes “unsorted” and can, if necessary, immediately move up a level to a shorter timestep. It can only move down a level to a longer timestep once the other particles on that level have completed their own *KDDK* step. Until then it remains at its existing timestep level.

The first call to `Kick` calculates the forces exerted by particles s_l, \dots, N on each other and updates their velocities

accordingly. This is equivalent to applying a kick obtained from the simple Hamiltonian (6) with $V = V_l + \dots + V_{l_{\max}}$ and $\tau = 2^{-l} \tau_0$, but the rules derived from the multistep Hamiltonian (11) demand a kick with $V = V_l$ only. So, this first `Kick` is followed immediately by a second one to remove the unwanted contribution from $V_{l+1} + \dots + V_{l_{\max}}$. Of course, the accelerations calculated in this second `Kick` can be reused immediately in the next call to `NBodyStep`.

Another important saving is that we do not need to include the full set of nested boxes in equation (3) when calculating the accelerations, because most of the particles $s_l \dots N$ will be inside boxes with timestep levels l or higher. If we make the safe assumption that particles never cross more than one box per timestep, then the full expression (3) for the accelerations felt by particles s_l, \dots, N can be written

$$\mathbf{a}(\mathbf{x}) = \mathbf{a}_i^+ + \sum_{j=i}^{j_{\max}} \mathbf{a}_j(\mathbf{x}), \quad (14)$$

where i is the *spatial* refinement level of the finest box that encloses all boxes having timestep level l or higher.

The final kick of each *KDDK* step is deferred to an ancillary function:

```

CompleteSteps( $l, \tau, \{s_i\}$ ):
  Kick( $\tau/2$ ) [ $s_l \dots N$ ]
  if  $l < l_{\max}$ :
    Kick( $-\tau/2$ ) [ $s_{l+1} \dots N$ ]
  CompleteSteps( $l+1, \tau/2, \{s_i\}$ )

```

This arranges the kicks in an order which makes it possible to calculate the accelerations efficiently.

4 TESTS AND COMPARISONS

I have carried out a number of simple tests with small numbers of particles ($1 < N \lesssim 20$) to confirm that my implementation of the ideas above really does respect Newton’s third law and conserve linear momentum. These small- N tests serve only as minimal sanity checks; as stressed by Knebe, Green & Binney (2001), truly interesting tests of a collisionless code come not from testing how faithfully it reproduces the solution to the two-body problem, but rather from its ability to model collisionless systems accurately using large numbers of particles.

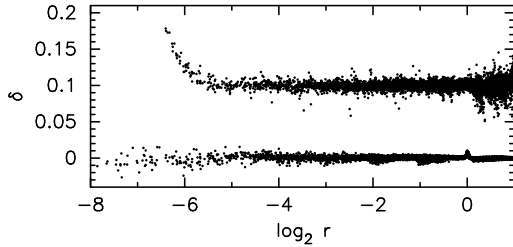


Figure 4. Fractional errors in the accelerations at randomly selected positions within and around an $N = 10^7$ -particle realization of a truncated power-law sphere. The lower set of points plot results calculated using the potential solver of section 2 using 8 levels of refinement of a 60^3 mesh with $x_{\max} = 2$. The upper set (offset by 0.1 vertically) are for results obtained using a tree code with fixed softening length $\epsilon = 10^{-2}$.

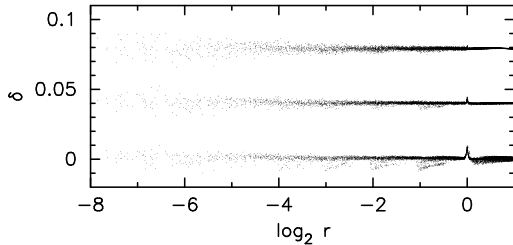


Figure 5. Fractional errors in the accelerations inside a 10^8 -particle realization of a power-law sphere, a factor 10 more particles than in figure 4. The lower set of points plot results obtained using the potential solver of section 2 with the same set of nested boxes and 60^3 mesh employed for figure 4. The middle and upper set show the effects of using finer meshes with 124^3 (middle) and 252^3 (upper) cells.

In this section I use some simple collisionless galaxy models to test Grommet's potential solver and integrator, comparing results obtained from Grommet against those obtained from two other codes. Both of the other codes are available as part of the NEMO package. The first is the fast tree code described in Dehnen (2002). It obtains accelerations from a Cartesian multipole expansion. This respects Newton's third law and a standard leapfrog integrator built around this potential solver then naturally conserves linear momentum. (A multiple-timestep version is also available, but it does not conserve momentum.) The second code (Hernquist & Ostriker 1992) uses the so-called "self-consistent field" (SCF) method, which represents the density and potential using a truncated basis function expansion. It shows no respect for Newton's third law, but, like Grommet, is optimized for modelling single galaxies.

4.1 Static tests

Real galaxies have steep central density cusps (e.g., Lauer et al. 1995), so an obvious test of the potential solver is to check the accelerations it returns for an N -body realization of a truncated power-law sphere with density profile

$$\rho(r) \propto \begin{cases} r^{-\alpha}, & \text{if } r < r_{\max}, \\ 0, & \text{otherwise.} \end{cases} \quad (15)$$

I have generated a realization with $r_{\max} = 1$, $\alpha = 2$ having 10^7 equal-mass particles and used eq. (3) to calculate accelerations at randomly selected positions inside and around the sphere. For this I use a toplevel box enclosing the region $|\mathbf{x}| < 2$ together with eight levels of refinement, the boundary of the i^{th} subbox being given by $|\mathbf{x}| = 2^{1-i}$. Figure 4 plots the fractional difference between the results of this procedure against the exact, analytical expression for the acceleration. For radii $2^{-5} < r < 1$ the RMS fractional error is only 0.0023, rising to 0.007 for $2^{-8} < r < 2^{-5}$, within which there are relatively few particles. The source of this good and desirable behaviour is the decrease in the effective softening length as one moves to smaller length scales.

For comparison, the upper set of points in figure 4 plot the errors in the accelerations of the same 10^7 -particle sphere calculated at the same positions using the tree code falcON with softening kernel P_2 and fixed softening length $\epsilon = 10^{-2}$. The RMS fractional error in the resulting accelerations for radii $2^{-5} < r < 1$ is 0.011, over four times larger than Grommet's, while for $r < 2^{-5}$, the calculated accelerations become systematically too low. falcON takes about 2.5 times longer than Grommet to produce these results and needs more than three times the memory.

Perhaps the most worrying feature of the nested box scheme of section 2 is that the accelerations (3) are discontinuous at box boundaries. One can see some hints of this discontinuity in figure 4 at $\log_2 r = -1, -2, -3$, but it is even clearer in figure 5 which plots the fractional errors in a 10^8 -particle realization. Even if one were to run a simulation with such large N , the discontinuity itself is unlikely to be important because the integration scheme in section 3.3 does not depend explicitly on the derivatives of the accelerations. More important is the fact that, if the discontinuity is noticeable, it means that the bias in the estimates of the accelerations has become significant. The natural solution is then to move to a finer mesh (e.g., 124^3 cells instead of 60^3 , figure 5).

4.2 Dynamical tests

For the dynamical tests I use a spherical isotropic Hernquist (1990) model with density profile

$$\rho(r) = \frac{Ma}{2\pi r(a+r)^3}. \quad (16)$$

This idealized model is in equilibrium. Then by Jeans' theorem (Binney & Tremaine 1987) its DF $f_0(\mathbf{x}, \mathbf{v})$ can depend on (\mathbf{x}, \mathbf{v}) only through the integrals of motion, which are the energy \mathcal{E} and angular momentum \mathbf{J} per unit mass. Since the model is isotropic the DF cannot depend on the latter and so $f = f_0(\mathcal{E})$.

A straightforward procedure for generating initial conditions (hereafter ICs) corresponding to this model would be to draw N particles directly from $f_0(\mathcal{E})$, assigning each a mass M/N . Integrating (16), the fraction of particles inside radius r would then be $r^2/(a+r)^2$, showing that there would be relatively few particles with radii $r \ll a$, deep inside the interesting r^{-1} central density cusp. To improve resolution near the centre, I instead generate initial conditions using a multi-mass scheme, drawing particles from an anisotropic sampling DF (Leeuw, Combes & Binney 1993) with num-

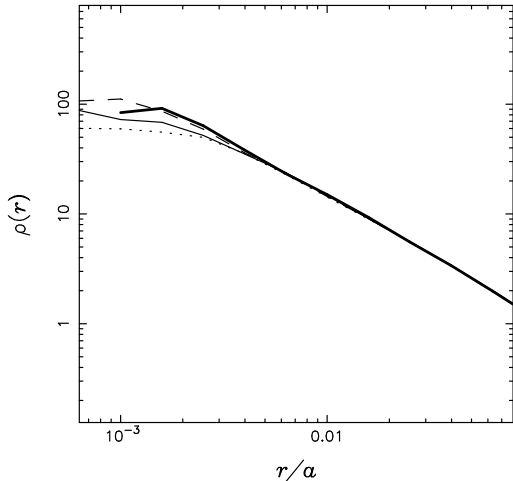


Figure 6. Inner density profile of the same realization of a Hernquist model after it has been evolved for 10 time units using a simple leapfrog integrator with accelerations obtained using different potential solvers: Grommet (light solid curve), **falcon** (dotted curve) and the SCF method (dashed). The heavy solid curve plots the density profile of the the initial conditions.

ber density

$$f_s(\mathcal{E}, J^2) = h(\mathcal{E}, J^2) f_0(\mathcal{E}), \quad (17)$$

where (Sigurdsson, Hernquist & Quinlan 1995)

$$h(\mathcal{E}, J^2) \equiv A \times \begin{cases} \left(\frac{r_{\text{peri}}}{a}\right)^{-\lambda} & \text{if } r_{\text{peri}} < a, \\ 1 & \text{otherwise,} \end{cases} \quad (18)$$

$r_{\text{peri}}(\mathcal{E}, J^2)$ is the particle's pericentre radius and the constant A is chosen to normalize f_s . When the parameter $\lambda = 0$, the sampling DF f_s is identical to $f_0(\mathcal{E})$. Increasing λ improves the sampling of the cusp by increasing the number density of particles having pericentres $r_{\text{peri}} < a$. To balance this increase in number density each particle is assigned a mass $M f_0 / N f_s = M / N h(\mathcal{E}, J^2)$ so that the phase-space mass density is still given by the desired $f_0(\mathcal{E})$.

For the tests below I adopt units $G = M = a = 1$ and draw 2×10^6 particles with radii in the range $10^{-3} < r < 10^2$ from the sampling DF (17) with $\lambda = 1$. Poisson noise in the resulting distribution of particles makes it slightly asymmetric, which has two unwanted consequences (see also McMillan & Dehnen 2005). First, the centre of mass of the system moves with a constant velocity of order $\sim 10^{-3} (GM/a)^{1/2}$ because the total linear momentum of the particles is small, but non-zero. Second, the asymmetry quickly destroys the inner part of the r^{-1} density cusp, even when viewed a frame co-moving with the centre of mass. To remove both of these effects, I extend my ICs to include the mirror distribution obtained by reflecting each of the 2×10^6 particles with $(\mathbf{x}, \mathbf{v}) \rightarrow (-\mathbf{x}, -\mathbf{v})$. The full ICs then have $N = 4 \times 10^6$ particles.

4.2.1 Evolution of an (almost) equilibrium model

Of course, one does not expect an N -body model evolved from these ICs to be in perfect equilibrium; the ICs omit particles outside the range $10^{-3} < r < 10^2$ and are constructed assuming the exact potential corresponding to the

Code	Time	Comment
falcon	2.1	single timestep
SCF	1.3	single timestep, $(n_{\text{max}}, l_{\text{max}}) = (6, 4)$
Grommet	1.0	single timestep
Grommet	0.4	four levels of timestep refinement
Grommet	0.19	seven levels of timestep refinement

Table 1. Comparison of time required for different codes to integrate the multi-mass Hernquist model of section 4.2, relative to the single-timestep implementation of Grommet. Neither the Grommet nor the SCF models take advantage of the reflection symmetry of this simple problem.

density distribution (16) instead of the softened potential used in the N -body code. Nevertheless, it is interesting to compare the evolution of the N -body model obtained from Grommet with those obtained from the other two codes.

Figure 6 shows the density profile of the models after 10 time units (or ~ 66 circular orbit periods at $r = 0.01$). All three models use the same simple leapfrog integrator with timestep 2×10^{-3} ; only the source of the accelerations is different. For Grommet I use boxes with boundaries at $|\mathbf{x}| = 100 \times 2^{-i}$ for $i = 0, \dots, 12$. Each box has 60^3 assignable cells, the cell length varying from 3.33 in the toplevel box down to 0.8×10^{-3} in the innermost box. falCON's results are obtained using kernel P_2 with softening length $\epsilon = 10^{-3}$, while the SCF expansion uses the Hernquist & Ostriker (1992) basis function expansion truncated at $n_{\text{max}} = 6$ radial and $l_{\text{max}} = 4$ angular terms.

The results plotted in figure 6 are unsurprising. The density at the very centre of the Grommet and falCON models falls slowly because because the ICs omit particles with radii $r < 10^{-3}$ and do not take into account the softening in these codes. In contrast, the density profile of the SCF model does not change significantly because its basis function expansion is incapable of producing anything that deviates strongly from a Hernquist model on small spatial scales.

Much more is happening at the level of individual orbits, however. All of these models begin with spherical symmetry and remain spherical, apart from the effects of Poisson noise. Therefore the amount of diffusion in the angular momentum J of their particles' orbits serves as a convenient measure of how far each code is from being perfectly collisionless. Figure 7 shows that the particles in all three models suffer from significant amounts of diffusion. The SCF model shows the least amount of diffusion, but it is only marginally better than Grommet; although the SCF potential remains close to the exact Hernquist potential, the flickering of the expansion coefficients with time makes the orbits diffuse just like in any other code. The diffusion is worst in the falCON model, particularly for orbits having pericentres much larger than its fixed softening length $\epsilon = 10^{-3}$. All of these results are based on the variation in orbits' angular momentum in models integrated from $t = 0$ to $t = 10$, but I find similar results for models integrated from, say, $t = 10$ to $t = 50$ when scaled to account for the longer timescale over which the diffusion occurs.

These results have been obtained an integrator with a single small timestep, but the dynamical time inside the cusp of a Hernquist model varies with radius r approximately as $r^{1/2}$. I find that a model evolved using the block-timestep integrator of section 3.3 with four levels of timestep

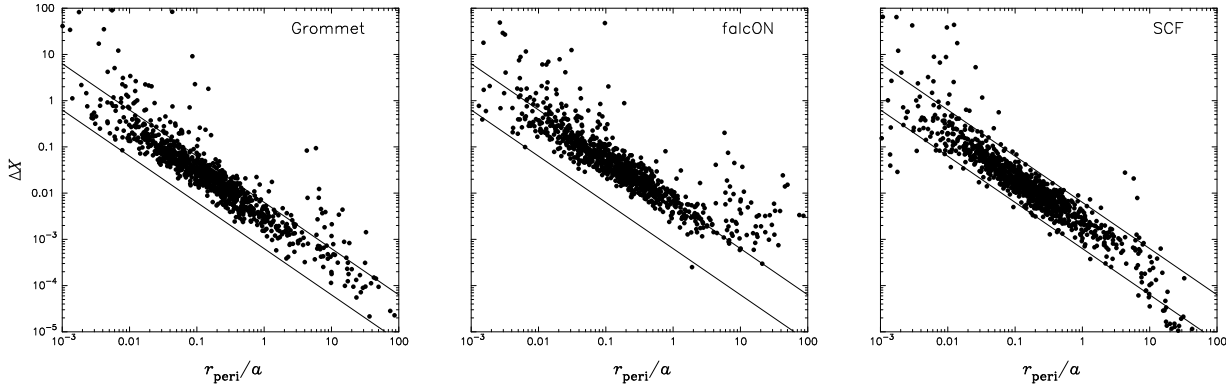


Figure 7. RMS spread in circularity $X \equiv J^2/J_{\text{circ}}^2(\mathcal{E})$ measured from $t = 0$ to $t = 10$ for a randomly selected set of particles in the models shown in figure 6, plotted as a function of the particles' pericentre radius. The same random selection of particles is used to generate each panel. $J_{\text{circ}}^2(\mathcal{E})$ and r_{peri} are calculated from the particles' ICs using the analytical potential corresponding to equation (16).

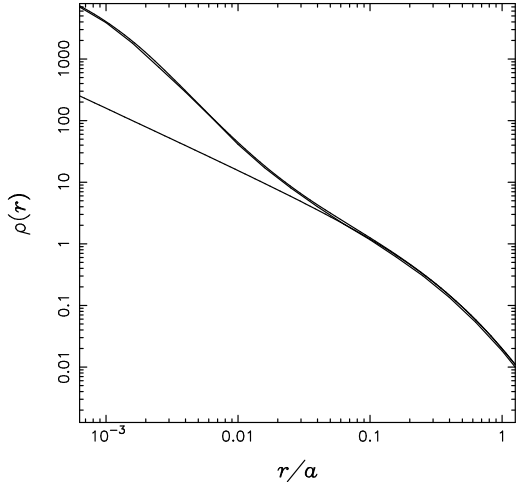


Figure 8. The results of adiabatically adding a Plummer sphere potential to an initially isotropic Hernquist model. The Plummer sphere has radius $2 \times 10^{-3}a$ and a final mass $2 \times 10^{-3} M_{\text{gal}}$. The results obtained using Grommet's multiple-timestep scheme are almost identical to those calculated from Young's (1980) method.

refinement yields results essentially identical to the single-timestep Grommet model plotted in figures 6 and 7. This multiple-timestep model uses a timestep 32×10^{-3} for particles with $|\mathbf{x}| > 100 \times 2^{-6} \simeq 1.5$. The timestep shrinks by a factor of two at the boundary $|\mathbf{x}| = 100 \times 2^{-i}$ of boxes $i = 6, 8, 10$ and 12 , so that the timestep in the innermost ($i = 12$) box is 2×10^{-3} , the same used for the single-timestep models. This multiple-timestep run is 2.5 times faster than the single-timestep run (see table 1). If it were appropriate to halve the timestep at *all* box boundaries $i = 6, \dots, 12$ (see below for an example) then using the block-timestep scheme would be five times faster than using the single-timestep integrator with the same timestep for the finest box.

4.2.2 Response to an adiabatically grown blob

For a slightly more interesting test, I model the growth of a black hole at the centre of a galaxy by slowly adding a

Plummer sphere potential

$$\Phi_b(\mathbf{x}; t) = -\frac{GM_b(t)}{\sqrt{r^2 + b^2}} \quad (19)$$

to a multi-mass Hernquist model. The scale radius of the Plummer sphere $b = 2 \times 10^{-3}$ and its mass grows with time as (Sigurdsson, Hernquist & Quinlan 1995)

$$M_b(t) = M_f \times \begin{cases} \left[3 \left(\frac{t}{t_g} \right)^2 - 2 \left(\frac{t}{t_g} \right)^3 \right] & \text{if } t < t_g \\ 1 & \text{otherwise,} \end{cases} \quad (20)$$

its final mass $M_f = 2 \times 10^{-3}$ being reached in a time $t_g = 5$.

A safe, formal way of including the effects of this external potential in Grommet is to add an extra term

$$V_b = \sum_i c(l_i, l_i) m_i \Phi_b(\mathbf{x}_i; t) \quad (21)$$

inside the double sum in the Hamiltonian (11). Integrating the resulting equations of motion then leads to the modifications needed in the block-timestep algorithm (section 3.3). In this case the necessary modifications are obvious, but for more realistic situations (e.g., if the mass of the external source did not change in time and if the location of its centre were not pinned to $\mathbf{x} = 0$) then it is helpful to start from (11) to ensure that momentum is conserved.

As above, I use a nested series of boxes with boundaries at $|\mathbf{x}| = 100 \times 2^{-i}$ with $i = 0, \dots, 12$, each box covered by a 60^3 mesh. Boxes 0 to 5 share a common timestep $\tau_0 = 5 \times 10^{-3}$. This is refined in every subsequent box, so that the timestep associated with box $i \geq 6$ is $2^{5-i}\tau_0$ and the innermost box ($|\mathbf{x}| < 0.24$) has timestep $\sim 4 \times 10^{-5}$.

My initial conditions consist of 10^6 particles drawn from the sampling DF (17) above. The artificially imposed potential at $\mathbf{x} = 0$ means that this simulation only makes sense if the particles' centre of mass is also at $\mathbf{x} = 0$. As an alternative to symmetrizing the ICs as before, I instead modify step (i) of the PM method (section 2) to reflect the particle distribution through each of the planes $\mathbf{x} = 0$, $\mathbf{y} = 0$, $\mathbf{z} = 0$ when assigning mass to meshes. This increases the effective N used for the potential by a factor of 8 at little cost. The density profile of the final model is plotted in figure 8. It agrees well with the predictions obtained using Young's (1980) method.

5 SUMMARY

I have described Grommet, a fast, economical particle-multiple-mesh N -body code designed specifically for modelling the dynamical evolution of individual galaxies. In other words, it is designed to tackle almost exactly the same type of problem to which the SCF method (Hernquist & Ostriker 1992) is applied. Indeed, Grommet can – loosely – be thought of as a variant of the SCF method using a Cartesian basis function expansion with millions of expansion coefficients (the density at each mesh vertex in each of the nested boxes).

For a realistic model galaxy with $N \gtrsim 10^6$, the single-timestep incarnation of Grommet is comparable in speed to an SCF code using a low-order basis expansion and shows comparable amounts of relaxation. For most applications, however, Grommet will be much faster: its nested-box potential solver admits an efficient natural block-timestep integrator (section 3.3), leading to an approximate two- to five-fold increase in speed; the SCF method typically requires a fairly high-order expansion to produce (reasonably) unbiased results (e.g., Holley-Bockelmann, Weinberg & Katz 2005), which will tend to make it slower. But perhaps the main advantage of Grommet over SCF methods based on spherical harmonic expansions is that it respects Newton’s third law and is therefore suitable for use in studying $l = 1$ perturbations without fear of artifacts due to centring.

To my knowledge, the tree code falcON (Dehnen 2002) is the only other code that can model realistically inhomogeneous galaxies without breaking the third law. For $N \gtrsim 10^6$ Grommet’s potential solver is more than twice as fast as falcON’s and much less memory hungry. Of course, this efficiency comes at a cost, since Grommet’s nested-box scheme is optimized for modelling perturbations of single galaxies. It would be interesting to see whether section 3.3’s momentum-conserving block-timestep scheme works as well for falcON (or indeed any other code that respects the third law) as it does for Grommet.

(The code will be made generally available on publication of this paper.)

ACKNOWLEDGMENTS

REFERENCES

Anninos P., Norman M. L., Clarke D. A., 1994, ApJ, 436, 11
 Binney J., Tremaine S., 1987, Galactic Dynamics, Princeton Univ. Press, Princeton, NJ
 Dehnen W., 2002, J. Comput. Phys., 179, 27
 Gelato S., Chernoff D. F., Wasserman I., 1997, ApJ, 480, 115
 Hernquist L., 1990, ApJ, 356, 359
 Hernquist L., Ostriker J. P., 1992, ApJ, 386, 375
 Hernquist L., Weinberg M. D., 1989, MNRAS, 238, 407
 Hockney R. W., Eastwood J. W., Computer simulation using particles, 1988, IoP
 Holley-Bockelmann K., Weinberg M., Katz N., 2005, MNRAS, 363, 991
 James R. A., 1977, J. Comp. Phys., 25, 71
 Jessop C., Duncan M., Chau, W. Y., 1994, J. Comput. Phys., 115, 339
 Knebe A., Green A., Binney J., 2001, MNRAS, 325, 845
 Kravtsov A. V., Klypin A. A., Khokhlov A. M., 1997, ApJS, 111, 73
 Lauer T. R., et al., 1995, AJ, 110, 2622
 Leeuw F., Combes F., Binney J., 1993, MNRAS, 262, 1013
 McMillan P. J., Dehnen W., 2005, MNRAS, 363, 1205
 Quinn T., Katz N., Stadel J., Lake G., arXiv preprint [astro-ph/9710043](http://arxiv.org/abs/astro-ph/9710043)
 Saha P., Tremaine S., 1992, AJ, 104, 1633
 Sigurdsson S., Hernquist L., Quinlan G. D., 1995, ApJ, 446, 75
 Velazquez H., White S. D. M., 1999, MNRAS, 304, 254
 Weinberg M. D., 1989, MNRAS, 239, 549
 Wisdom J., Holman M., 1991, AJ, 102, 1528
 Young P., 1980, ApJ, 242, 1232

APPENDIX A: JAMES’ METHOD

James (1977) describes an economical method for calculating the solution to Poisson’s equation,

$$\nabla^2 \Phi = -q, \quad (A1)$$

discretized on a regular mesh and with a spatially bounded source distribution $q(\mathbf{x})$, so that $\partial\Phi/\partial\mathbf{r} \rightarrow 0$ as $r \rightarrow \infty$. It is easiest to explain his method for the electrostatic case in which q is electric charge density and Φ is electrostatic potential. The method then consists of the following steps:

- (i) enclose the charge distribution q inside an earthed metal box and calculate the potential $\phi(\mathbf{x})$ inside the box subject to the boundary condition $\phi = 0$ on the box surface;
- (ii) use Gauss’ law to find the charge distribution Q induced on the surface of the box;
- (iii) calculate the potential $\psi(\mathbf{x})$ due to this surface charge distribution Q .

The solution to (A1) for the isolated charge distribution q is given by $\Phi = \phi - \psi$. Since this procedure is at the heart of Grommet’s potential solver, I explain it in some detail below.

A1 Preliminaries

Throughout the following, I assume that the distribution $q(\mathbf{x})$ has been discretized onto a cubical mesh with vertices at positions $\mathbf{x}_{ijk} = (i, j, k)$, $0 \leq i, j, k \leq n$, spaced unit distance apart. Our goal is to calculate the discretized potential Φ_{ijk} corresponding to this q_{ijk} .

A straightforward way of doing this is to use the Fourier convolution theorem. Consider first the situation in which the charge distribution q_j is one-dimensional with $0 \leq j < 2n$; the reason for extending the mesh from $n + 1$ to $2n$ vertices will become apparent shortly. The discretized potential is given by the convolution

$$\Phi_j = \sum_{k=0}^{2n-1} G_k q_{k-j}, \quad (A2)$$

where G_k is the contribution to Φ_k made by a unit-charge particle located at x_0 , and we take $q_k = 0$ for $k < 0$ or $k \geq 2n$ since we have an isolated charge distribution.

This last condition on q is awkward. Suppose instead that both that G_k and q_k were $2n$ -periodic, with $q_{-k} = q_{2n-k}$, and let us impose the sensible condition that G_k is even with $G_k = G_{2n-k}$ and that $G_0 = 0$. Then Φ_j could be obtained economically using Fourier methods. The Fourier transform of q_i is given by

$$q^\alpha \equiv \sum_{j=0}^{2n-1} q_j \exp \left[\frac{i\pi j\alpha}{n} \right], \quad (\text{A3})$$

where $i \equiv \sqrt{-1}$, and similarly for G^α . Using the discrete convolution theorem, equation (A2) becomes simply

$$\Phi^\alpha = G^\alpha q^\alpha. \quad (\text{A4})$$

Applying the inverse transform, the potential is given by

$$\Phi_j = \frac{1}{2n} \sum_{\alpha=0}^{2n-1} \Phi^\alpha \exp \left[-\frac{i\pi j\alpha}{n} \right]. \quad (\text{A5})$$

Of course, the periodicity needed for application of the discrete convolution theorem is a nuisance, but if we allow q_i to be non-zero only for $0 \leq i \leq n$, then the $\Phi_0 \dots \Phi_n$ obtained from equ. (A2) are unaffected by it. Therefore, we can use this Fourier method to obtain the potential Φ_i corresponding to an isolated source distribution q_i ($0 \leq i \leq n$) provided we extend the mesh by a further $n-1$ points with $q_{n+1} = \dots = q_{2n-1} = 0$. Thanks to the existence of fast methods for evaluating the transforms (A3) and (A5), the Fourier method requires only $\mathcal{O}(n \log n)$ operations to calculate the full set of Φ_i , instead of the $\mathcal{O}(n^2)$ involved in a direct evaluation of equ. (A2). The savings are much more dramatic for the three-dimensional case, for which the direct sum takes $\mathcal{O}(n^6)$ operations, compared to only $\mathcal{O}((n \log n)^3)$ for the Fourier method.

James' method makes use of an alternative view of this “doubling up” procedure. The Fourier transform (A3) can be written as

$$q^\alpha = 2[q^\alpha(C) + iq^\alpha(S)], \quad (\text{A6})$$

where the cosine and sine transforms

$$q^\alpha(C) \equiv \sum_{j=0}^n c_j q_j \cos \frac{\pi j\alpha}{n}, \quad (\text{A7})$$

$$q^\alpha(S) \equiv \sum_{j=1}^{n-1} q_j \sin \frac{\pi j\alpha}{n}, \quad (\text{A8})$$

come from the even and odd parts of q_j ,

$$q_j^\pm \equiv \frac{1}{2} (q_j \pm q_{2n-j}), \quad (\text{A9})$$

respectively. The coefficients $c_1 = \dots = c_{n-1} = 1$, but $c_0 = c_n = \frac{1}{2}$ to account for the fact that q_0 and q_n are counted only half as often as the other q_i . Conversely, having both $q^\alpha(C)$ and $q^\alpha(S)$ we can reconstruct the original q_j by substituting (A6) into the expression for the inverse transform (A5) to obtain

$$q_j = q_j(C) + q_j(S), \quad (\text{A10})$$

where

$$q_j(C) \equiv \frac{2}{n} \sum_{\alpha=0}^n c_\alpha q^\alpha(C) \cos \frac{\pi j\alpha}{n}, \quad (\text{A11})$$

$$q_j(S) \equiv \frac{2}{n} \sum_{\alpha=1}^{n-1} q^\alpha(S) \sin \frac{\pi j\alpha}{n} \quad (\text{A12})$$

are the inverse cosine and sine transforms of $q^\alpha(C)$ and $q^\alpha(S)$ respectively. Thus, apart from a factor of $(2/n)$, the cosine and sine transforms are their own inverses.

Now suppose that only $q_0 \dots q_n$ are allowed to be non-zero. Then $q_i^+ = q_i^- = q_i$, except for the unused $q_0^- = q_n^- = 0$. Replacing q by Φ in equs. (A10-A12) and taking Φ^α from (A4), the potential can be written as

$$\Phi_j = \Phi_j(C) + \Phi_j(S), \quad (\text{A13})$$

where

$$\Phi_j(C) \equiv \frac{2}{n} \sum_{\alpha=0}^n c_\alpha G^\alpha q^\alpha(C) \cos \frac{\pi j\alpha}{n}, \quad (\text{A14})$$

$$\Phi_j(S) \equiv \frac{2}{n} \sum_{\alpha=1}^{n-1} G^\alpha q^\alpha(S) \sin \frac{\pi j\alpha}{n}, \quad (\text{A15})$$

and $G^\alpha = 2G^\alpha(C)$ with no contribution from the sine transform of the even function G_i .

The generalization to three dimensions is straightforward. The Fourier transform in each direction splits into a sum of cosine and sine terms, yielding a total of eight terms:

$$\begin{aligned} \Phi_{ijk} = & \Phi_{ijk}(CCC) + \Phi_{ijk}(CCS) + \Phi_{ijk}(CSC) \\ & + \Phi_{ijk}(CSS) + \Phi_{ijk}(SCC) + \Phi_{ijk}(SCS) \\ & + \Phi_{ijk}(SSC) + \Phi_{ijk}(SSS), \end{aligned} \quad (\text{A16})$$

where, for example,

$$\begin{aligned} \Phi_{ijk}(CSS) \equiv & \frac{8}{n^3} \sum_{i=0}^n \sum_{j=1}^{n-1} \sum_{k=1}^{n-1} c_i \Phi^{\alpha\beta\gamma}(CSS) \times \\ & \cos \frac{\pi i\alpha}{n} \sin \frac{\pi j\beta}{n} \sin \frac{\pi k\gamma}{n}, \end{aligned} \quad (\text{A17})$$

with $\Phi^{\alpha\beta\gamma}(CSS) = G^{\alpha\beta\gamma} q^{\alpha\beta\gamma}(CSS)$ and

$$\begin{aligned} q^{\alpha\beta\gamma}(CSS) \equiv & \sum_{i=0}^n \sum_{j=1}^{n-1} \sum_{k=1}^{n-1} c_i q_{ijk} \cos \frac{\pi i\alpha}{n} \sin \frac{\pi j\beta}{n} \sin \frac{\pi k\gamma}{n}. \end{aligned} \quad (\text{A18})$$

Notice that this decomposition into sine and cosine transforms results in two transforms for each of eight n^3 meshes. It requires less memory than the equivalent single $(2n)^3$ zero-padded mesh used in the “doubling-up” procedure, but for general q_{ijk} and G_{ijk} it offers no improvement in speed. It simplifies enormously, however, for the special case in which G_{ijk} is the Green’s function of the discretized Laplacian appearing in equ. (A1). James’ method exploits these simplifications, particularly in dealing with the hollow induced surface charge distribution Q (see section A4 below).

A2 The potential of a charge distribution inside an earthed box

With this background in hand, let us turn to the details of James’ method. Poisson’s equation (A1) can be written

$$(\Delta\Phi)_{ijk} = -q_{ijk} \quad (\text{A19})$$

where the first-order approximation to the Laplacian operator

$$\begin{aligned} (\Delta\Phi)_{ijk} \equiv & \Phi_{i+1,j,k} + \Phi_{i-1,j,k} + \Phi_{i,j+1,k} + \Phi_{i,j-1,k} + \\ & + \Phi_{i,j,k+1} + \Phi_{i,j,k-1} - 6\Phi_{ijk}. \end{aligned} \quad (\text{A20})$$

The potential ϕ_{ijk} of the earthed box is given by the solution of this equation subject to the boundary condition $\phi_{0jk} = \phi_{njk} = \phi_{iok} = \phi_{ink} = \phi_{ijo} = \phi_{ijn} = 0$. Applying the triple sine transform, we have that

$$\phi^{\alpha\beta\gamma}(SSS) = q^{\alpha\beta\gamma}(SSS)/C^{\alpha\beta\gamma} \quad (\text{A21})$$

where

$$C^{\alpha\beta\gamma} = 2 \left(1 - \cos \frac{\pi\alpha}{n} \right) + 2 \left(1 - \cos \frac{\pi\beta}{n} \right) + 2 \left(1 - \cos \frac{\pi\gamma}{n} \right). \quad (\text{A22})$$

Although we could immediately apply the inverse transform (A16) to obtain ϕ_{ijk} explicitly, it turns out that this is unnecessary and it is more efficient to use the method of equivalent charges (see below) to modify $\phi^{\alpha\beta\gamma}(SSS)$ to include the effects of the potential ψ corresponding to the induced surface charge distribution Q , saving everything for a single inverse transform at the very end of the calculation.

A3 The charge distribution induced on the faces of the box

The charge distribution induced on the $i = 0$ face of the box is given by

$$Q_{0jk} = -(\Delta\phi)_{0jk} = -\phi_{1jk}, \quad (\text{A23})$$

the last equality following from the fact that ϕ is zero both on the box surface ($i = 0$) and outside the box ($i = -1$). Similarly, the charge distribution induced on the opposite $i = n$ face is $Q_{njk} = \phi_{n-1,jk}$. Notice that Q vanishes along the edges of the box, and so is completely specified by its double sine transform on each of the six faces. In terms of $\phi^{\alpha\beta\gamma}(SSS)$ these can be written

$$Q_0^{\beta\gamma}(SS) = \frac{2}{n} \sum_{\alpha=1}^{n-1} \phi^{\alpha\beta\gamma}(SSS) \sin \frac{\pi\alpha}{n}, \quad (\text{A24})$$

$$Q_n^{\beta\gamma}(SS) = \frac{2}{n} \sum_{\alpha=1}^{n-1} (-1)^\alpha \phi^{\alpha\beta\gamma}(SSS) \sin \frac{\pi\alpha}{n}, \quad (\text{A25})$$

and similarly for the other four faces. We can invert each of these to obtain Q_{0jk} etc and, from these, any of the other three transforms $Q_0^{\beta\gamma}(SC)$, $Q_0^{\beta\gamma}(CC)$, $Q_0^{\beta\gamma}(CS)$.

A4 The potential of the induced charge distribution

Equation (A16) provides a way of obtaining the potential ψ_{ijk} corresponding to this induced charge distribution Q . The result is a sum of eight terms, all of which can be treated in the same way. For example, consider the term $\psi_{ijk}(CSS)$. Its Fourier transform $\psi^{\alpha\beta\gamma}(CSS) = G^{\alpha\beta\gamma}Q^{\alpha\beta\gamma}(CSS)$, where, using (A18) and the hollowness of Q ,

$$Q^{\alpha\beta\gamma}(CSS) = Q_0^{\beta\gamma}(SS) + (-1)^\alpha Q_n^{\beta\gamma}(SS). \quad (\text{A26})$$

The other terms can be written in a similar way, although the SSS term vanishes. The $G^{\alpha\beta\gamma}$ used here should the triple cosine transform of the Green's function for the first-order Laplacian (A20). This need be calculated (e.g., using the doubling-up procedure) just once, the necessary elements (next paragraph) being stored for subsequent use.

It would be possible to use eq. (A16) to obtain ψ_{ijk} directly, but it turns out (see below) that this labour is unnecessary and that it suffices to use (A16) to obtain only the face potentials ψ_{0jk} , ψ_{njk} etc. Nevertheless, adding up all the contributions to each of these turns out to be the main computational burden of James' method.

A5 The method of equivalent charges

Instead of synthesizing ψ_{ijk} explicitly, let us introduce another potential $\psi_{ijk}^{(E)}$ which is zero on the box faces but everywhere else is equal to ψ_{ijk} . Because it vanishes at the box boundaries, this new potential is completely specified by its triple sine transform. The "equivalent charge" distribution E_{ijk} that generates it can be found using Poisson's equation

$$\nabla^2 [\psi - \psi^{(E)}] = -[Q - E], \quad (\text{A27})$$

where Q is non-zero only on the faces of the box. For the first-order discretized Laplacian (equ. A20) E is confined to the planes $i = 1, j = 1, k = 1, i = n - 1, j = n - 1$ and $k = n - 1$, with, for example, $E_1^{\beta\gamma}(SS) = \psi_0^{\beta\gamma}(SS)$.

The triple sine transform of the full potential is then

$$\Phi^{\alpha\beta\gamma}(SSS) = \phi^{\alpha\beta\gamma}(SSS) - E^{\alpha\beta\gamma}(SSS)/C^{\alpha\beta\gamma} \quad (\text{A28})$$

the second term giving the contribution of $\psi^{(E)}$. Applying the inverse triple-sine transform to (A28) gives Φ_{ijk} for $1 \leq i, j, k < n$. Finally, the missing face potentials can be inserted using the results obtained in section A4.

A6 Performance

My implementation of this procedure uses the fast sine and cosine transforms written by Takuya Ooura.² The triple-sine transforms involved in going from q_{ijk} to $\phi^{\alpha\beta\gamma}(SSS)$ (eq. A21) and from $\Phi^{\alpha\beta\gamma}(SSS)$ to Φ_{ijk} (eq. A28) then take only $\sim 30\%$ of the total time needed to go from q_{ijk} to Φ_{ijk} , with the evaluation of the various transforms of the face charge distributions (Sec. A3) accounting for a further 10%. The remaining 60% of the time is spent simply accumulating the various contributions to the face potentials (sec. A4). Nevertheless, for typical 65^3 or 129^3 meshes I find that my implementation of James' method is about 60 to 70% faster than the usual doubling-up procedure.

I have focused here on describing James' method using the first-order approximation of the Laplacian (A20). James (1977) shows how it is possible to apply the same ideas to higher-order approximations, albeit at the expense of much more involved book-keeping. I find that the resulting minor changes in the Green's function G_{ijk} have no detectable effect for the realistic large- N situations described in section 4.

² <http://momonga.t.u-tokyo.ac.jp/~ooura/fft.html>